The Astrophysical Journal, 905:120 (9pp), 2020 December 20 https://doi.org/10.3847/1538-4357/abc74b


# A Dust Trap in the Young Multiple System HD 34700

Peyton Benac[1], Luca Matrà[1,2], David J. Wilner[1], Marìa J. Jimènez-Donaire[3], J. D. Monnier[4], Tim J. Harries[5], Anna Laws[5], Evan A. Rich[4], and Qizhou Zhang[1]
[1] Harvard-Smithsonian Center for Astrophysics, Cambridge, MA 02139, USA
[2] School of Physics, National University of Ireland Galway, University Road, Galway, Ireland
[3] Observatorio Astronómico Nacional, Alfonso XII 3, E-28014, Madrid, Spain
[4] Astronomy Department, University of Michigan, Ann Arbor, MI 48109, USA
[5] Department of Physics and Astronomy, University of Exeter, Exeter, EX4 4QL, UK
*Received 2020 July 25; revised 2020 November 1; accepted 2020 November 2; published 2020 December 21*

## Abstract

Millimeter observations of disks around young stars reveal substructures indicative of gas pressure traps that may aid grain growth and planet formation. We present Submillimeter Array observations of HD 34700: two Herbig Ae stars in a close binary system (Aa/Ab, ∼0.25 au), surrounded by a disk presenting a large cavity and spiral arms seen in scattered light, and two distant, lower-mass companions. These observations include 1.3 mm continuum emission and the $^{12}$CO 2–1 line at ∼0.″5 (178 au) resolution. They resolve a prominent azimuthal asymmetry in the continuum and Keplerian rotation of a circumbinary disk in the $^{12}$CO line. The asymmetry is located at a radius of $155^{+11}_{-7}$ au, consistent with the edge of the scattered-light cavity, being resolved in both radius ($72^{+14}_{-15}$ au) and azimuth (FWHM = $64^{\circ+8}_{-7}$). The strong asymmetry in millimeter continuum emission could be evidence for a dust trap, together with the more symmetric morphology of $^{12}$CO emission and small grains. We hypothesize an unseen circumbinary companion responsible for the cavity in scattered light and creating a vortex at the cavity edge that manifests in dust trapping. The disk mass has limitations imposed by the detection of $^{12}$CO and nondetection of $^{13}$CO. We discuss its consequences for the potential past gravitational instability of this system, likely accounting for the rapid formation of a circumbinary companion. We also report the discovery of resolved continuum emission associated with HD 34700B (projected separation ∼1850 au), which we explain through a circumstellar disk.

*Unified Astronomy Thesaurus concepts:* Protoplanetary disks (1300); Circumstellar disks (235); Planetary system formation (1257); Circumstellar dust (236); Interferometry (808); Submillimeter astronomy (1647)

## 1. Introduction

In recent years, protoplanetary disks have been shown to contain substructures in the form of spiral arms, rings, cavities, and asymmetries (e.g., Andrews et al. 2018). In many systems, prominent spiral arms are observed in the infrared, while a more concentrated and strongly asymmetric congregation of dust grains is seen in (sub)millimeter wavelengths, e.g., IRS 48, V 1247 Ori, LkHα 330, MWC 758, HD 142527, and HD 135344B (Casassus et al. 2012, 2013, 2015; Isella et al. 2013; van der Marel et al. 2013; Follette et al. 2015; Marino et al. 2015; Akiyama et al. 2016; Fuente et al. 2017; Kraus et al. 2017; Cazzoletti et al. 2018). These (sub)millimeter azimuthal asymmetries are considered evidence of dust trapping, as proposed by Whipple (1972), Weidenschilling (1977), and Barge & Sommeria (1995). When a local pressure maximum arises, large dust grains drift toward it and grow. By preventing radial drift of large grains into the star, these pressure maxima become a site of efficient dust growth, potentially leading to planetesimal formation. Evidence of strong azimuthal dust trapping in a protoplanetary disk was first observed by van der Marel et al. (2013) in (sub)millimeter observations of the system Oph IRS 48. Because thermal emission observations typically probe grains of a size comparable to the observing wavelength, (sub)millimeter observatories like the Submillimeter Array (SMA) are uniquely able to image the compact emission that arises from the enhanced clumping of large dust grains (Beckwith et al. 1990; Testi et al. 2003).

The multiple system HD 34700 is comprised of a binary Herbig Ae system (HD 34700AaAb, with a semimajor axis of $a \sim 0.25$ au based on the spectroscopic observations of Torres 2004) and a distant tertiary companion, HD 34700B, located at a projected distance of ∼1850 au from the central binary, as well as another companion, HD 34700C, at a projected separation of 3300 au (Sterzik et al. 2005). The central binary is composed of two close, young stars, of age ∼5 Myr and mass ∼2 $M_{\odot}$, orbiting with a period of approximately 23 days and an eccentricity of ∼0.25 (Torres 2004; Monnier et al. 2019). The new distance determination from Gaia Collaboration et al. (2018) revised the previously uncertain distance to the system to be 356.5 ± 6.1 pc, which significantly reduced the estimate of the age of the system (Monnier et al. 2019). This revised age indicates that the disk is a transition disk around a pair of young stars, not a debris disk around an older main-sequence star. The shape of the spectral energy distribution suggested a cavity around the central binary, which was confirmed by near-IR (NIR) GPI observations presented in Monnier et al. (2019). These NIR scattered-light observations resolved the disk around the central binary for the first time, unveiling a large, ∼175 au cavity and multiple spiral arms in a circumbinary disk with an inclination of ∼42° and elongation along a position angle of ∼69° E of N (Monnier et al. 2019). New Subaru/SCExAO +CHARIS observations (Uyama et al. 2020) yielded *JHK*-band images that confirmed the ring structure and spirals imaged with GPI in Monnier et al. (2019). These observations revealed darkening on the ring and spirals and were used to set limits on the mass of potential companions (Uyama et al. 2020). These scattered-light observations trace the (sub)micron grain population in the upper layers of the disk (e.g., Juhász & Rosotti 2018). These small grains are least susceptible to congregating in pressure maxima (Weidenschilling 1977). Therefore, we use (sub)millimeter observations to probe the distribution of larger,

**Table 1**
SMA Observational Parameters

| Parameter (1) | 2019 January 8 (2) | 2019 March 2 (3) | 2019 March 4 (4) |
|---|---|---|---|
| No. antennas | 8 | 7 | 8 |
| Configuration | SUB | VEX | VEX |
| $\tau_{225}$ | 0.04 | 0.04 | 0.03 |
| Min./max. baselines | 9–69 m | 68–508 m | 68–508 m |
| Gain calibrators | 0510+180, 0532+075 | 0509+056, 0532+075 | 0509+056, 0532+075 |
| Passband calibrators | 3c84 | 3c279, 3c84 | 3c279, 3c84 |
| Flux calibrator | Uranus | Uranus | Uranus |
| Synthesized beam FWHM | $4\farcs4 \times 3\farcs4$ | $0\farcs58 \times 0\farcs41$ | $0\farcs58 \times 0\farcs41$ |

millimeter-sized grains that lie closer to the circumbinary disk's midplane.

In this paper, we present new SMA subarcsecond-resolution observations of the HD 34700 system. In Section 2, we describe the observations and data products. In Sections 3 and 3.1, we present the results of the imaging and model fits to the visibilities that characterize the observed features. In Section 4, we discuss the interpretations and possible origins of these features. In Section 5, we summarize the conclusions.

## 2. Observations

We used the SMA[6] (Ho et al. 2004) to image the continuum, $^{12}$CO, and $^{13}$CO $J = 2$–1 emission in the HD 34700 system at high angular resolution. Observations in the very extended (VEX) configuration were performed on 2019 March 2 and 4. Subcompact (SUB) observations, which did not cover the $^{13}$CO line, were performed on 2019 January 7 to provide additional information about the possible presence of large-scale structures filtered out by the long VEX baselines. A summary of the observational parameters is available in Table 1. Observations are centered at R.A. 05:19:41.4097, decl. +05:38:42.8037 (J2000), which is the expected position of the central binary based on Gaia coordinates and proper motion extrapolated to the date of observation (Gaia Collaboration et al. 2018). The spectral setup of the VEX observations was centered at the local oscillator frequency of 225 GHz. The frequencies covered in the spectral observations were 229–237 GHz in the upper sideband and 213–221 GHz in the lower sideband. The main spectral line of interest in these observations was $^{12}$CO $J = 2$–1, located at a rest frequency of 230.538 GHz. The primary beam FWHM in these observations was $55\farcs0$.

Calibration of the interferometric visibilities was performed using the MIR[7] software package. Corrections were made for system temperature, and the calibrators listed in Table 1 were used for gain, passband, and flux calibration. Imaging and deconvolution were performed using the *tclean* task in the Common Astronomy Software Applications (CASA) package (McMullin et al. 2007). Before imaging the continuum, the visibilities at the frequency of the known CO transition were flagged and excluded. The continuum imaging was performed using a natural weighting scheme with no taper. The continuum image has an rms of 0.19 mJy beam$^{-1}$ with a synthesized beam size of $0\farcs58 \times 0\farcs41$. At the Gaia-determined distance of 356.5 pc, this translates to a resolved physical scale of 210 × 150 au. When referring to a radius, we always refer to radii in the orbital plane (i.e., deprojected), rather than on-sky radii.

In order to image the CO emission, the continuum emission was subtracted using the *uvcontsub* task in CASA. The $^{12}$CO and $^{13}$CO lines were also cleaned with natural weighting with no taper. The $^{12}$CO ($^{13}$CO) cube was produced with a channel width of 0.73 (1) km s$^{-1}$ and a single-channel rms noise level of 30 (25) mJy beam$^{-1}$ for a synthesized beam of $0\farcs56 \times 0\farcs40$ ($0\farcs57 \times 0\farcs40$).

The images presented use the VEX observations only, but the SUB data are included in the visibility modeling performed in Section 3.1. As shown by our visibility modeling in Section 3.1, these VEX observations recover all of the flux detected in the very compact configuration SUB observations. Therefore, these images provide the highest angular resolution for the resolved morphologies, without the complexities introduced into the synthesized beam shape by the large gap in $u$, $v$ coverage between the VEX and SUB baselines.

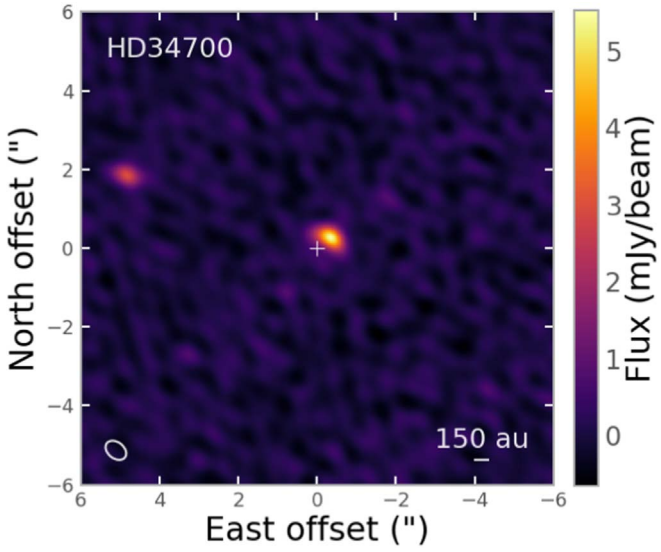


**Figure 1.** Cleaned dust continuum image ($\lambda = 1.3$ mm) of the HD 34700 multiple system obtained with natural weighting using the VEX data. The white ellipse at lower left represents the synthesized beam size of $0\farcs58 \times 0\farcs41$. The plus sign denotes the location of the central binary as determined from Gaia coordinates and proper motion, corresponding to the phase center of our observations.

## 3. Results

Figure 1 shows the SMA 1.3 mm continuum image of the HD 34700 system. This shows prominent emission next to but offset from the central binary, which was located at the phase center of our observations, corresponding to the [0,0] location. The continuum emission is detected with a peak signal-to-noise ratio (S/N) of 30.6 and a total integrated flux of 7.4 ± 1.6 mJy, including a 20% flux calibration uncertainty added in quadrature. Given the S/N of the azimuthally asymmetric emission, the contrast against undetected emission (if any) at other azimuthal locations is at least 10.2. The dust continuum emission around

[6] The SMA is a joint project between the Smithsonian Astrophysical Observatory and the Academia Sinica Institute of Astronomy and Astrophysics and is funded by the Smithsonian Institution and the Academia Sinica.
[7] https://www.cfa.harvard.edu/~cqi/mircook.html

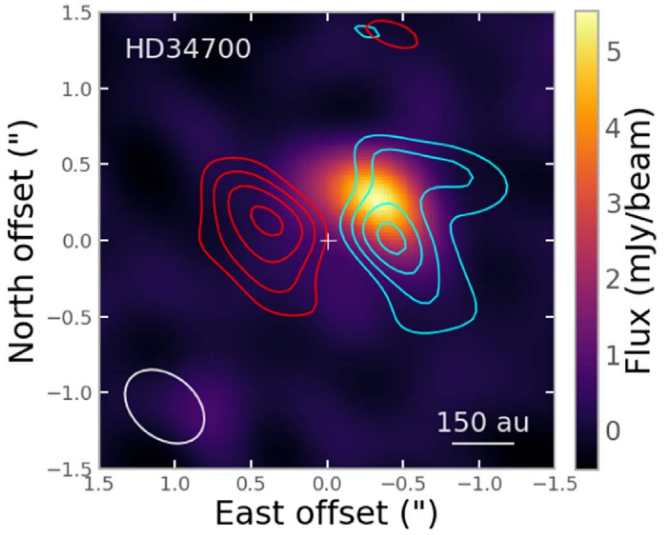


**Figure 2.** Contours represent the CO $J = 2$–1 moment-zero emission from blue- and red- shifted velocity with respect to the HD 34700AaAb binary's systemic velocity of 21 km s$^{-1}$ in the heliocentric reference frame (Pourbaix et al. 2004). Blueshifted emission includes emission from 17 to 21 km s$^{-1}$, and redshifted emission is from 21 to 25 km s$^{-1}$. Contours are drawn at 4, 6, 8, and 10 times the rms of the CO moment-zero map (49 mJy beam$^{-1}$ km s$^{-1}$) and overlaid on a zoomed-in version of the dust continuum image of Figure 1. The continuum beam size of $0\farcs58 \times 0\farcs41$ is shown in the ellipse at lower left.

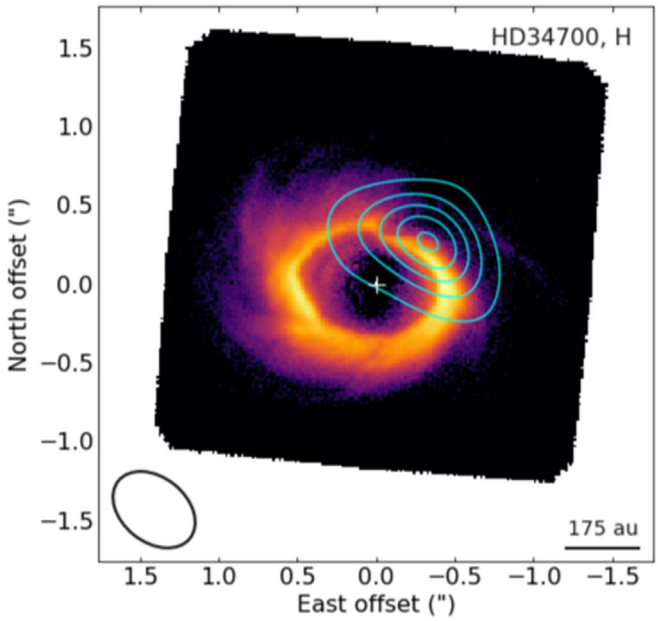


**Figure 3.** The *H*-band GPI image of the circumbinary disk around HD 34700AaAb as presented in Monnier et al. (2019), overlaid with contours of the SMA 1.3 mm continuum observations. The GPI image shows the radial Stokes component $Q_\phi$ (as defined in, e.g., Schmid et al. 2006; Monnier et al. 2019) plotted on a logarithmic color scale. Contours represent 3, 7, 11, 15, and 19 times the continuum rms of 0.19 mJy beam$^{-1}$. The plus sign denotes the expected location of the central binary. The continuum beam size of $0\farcs58 \times 0\farcs41$ is shown in the ellipse at lower left.

the central binary overlaps with the spiral structures observed in scattered light by Monnier et al. (2019), as shown in Figure 3.

We also detect significant emission at a location consistent with that of the distant companion HD 34700B, as shown in Figure 1. This emission has a peak S/N of 16.7 and an integrated flux of 3.7 ± 0.9 mJy, including the same 20% flux calibration uncertainty. This emission is likely to originate from a previously unknown protoplanetary disk around the tertiary companion HD 34700B.

The contours in Figure 2 show the integrated intensity $^{12}$CO emission from blue- and redshifted velocities with respect to the star's velocity of 21 km s$^{-1}$ in the heliocentric reference frame (Pourbaix et al. 2004). This emission is consistent with the expected velocity pattern of a Keplerian disk and well centered on the location of the central binary as determined from optical observations (Gaia Collaboration et al. 2018). This confirms the proper positioning of the central binary at phase center and therefore that the offset of the continuum emission shown in Figure 1 must have a physical origin and is not due to an astrometric error. The $^{12}$CO emission has a total integrated flux of 7.2 ± 1.4 Jy km s$^{-1}$. No $^{12}$CO emission is detected at the location of HD 34700B, and no $^{13}$CO emission is detected around both HD 34700AaAb and B. To set an upper limit on the $^{13}$CO integrated line flux around AaAb, we spatially integrate the cube over the same region where $^{12}$CO is detected (assuming they would be colocated) to obtain a 1D spectrum with an rms noise level of 93 mJy in a 1 km s$^{-1}$ channel. We then calculate a 3$\sigma$ spectrally integrated $^{13}$CO flux upper limit of 0.79 Jy km s$^{-1}$ by assuming that the two isotopologues have the same line width.

To estimate the spatial extent of the CO emission, we measure the spatial centroid of the highest-velocity channels where $^{12}$CO is detected using the *imfit* CASA task. Assuming a position angle for the disk major axis of 69° (Monnier et al. 2019), the CO is detected down to a separation of 102 ± 10 au from the central binary, which is significantly smaller than the radial location of the trap and the bright IR ring as imaged in Monnier et al. (2019). This is consistent with other transition disks with large cavities, where CO gas is detected interior to the cavity seen in dust emission (e.g., Bruderer et al. 2014; van der Marel et al. 2018), as predicted by models of massive planet-induced gaps (e.g., Pinilla et al. 2012). Higher-resolution line observations are needed to study the detailed interplay of gas and dust dynamics at the cavity edge.

### 3.1. Modeling

The asymmetric emission detected near the central AaAb binary was modeled as a geometrically thin, radially Gaussian ring with an azimuthal asymmetry according to Equation (1), following the vortex prescription of Lyra & Lin (2013), and successfully used in the modeling of higher-resolution ALMA observations of the dust trap around HD 135344B (Cazzoletti et al. 2018):

$$I(r, \theta) = A e^{\frac{-(r-r_c)^2}{2\sigma_r^2}} e^{\frac{-(\theta-\theta_c)^2}{2\sigma_\theta^2}}. \quad (1)$$

This model only includes the asymmetric crescent-shaped signal seen in the middle panel of Figure 4, not a full circumbinary disk. The dust emission around the companion HD 34700B was modeled as a Gaussian centered on the star with an offset from the phase center of our visibility data. We create model images from these intensity distributions. We used the *GALARIO* software package (Tazzari et al. 2018) to Fourier-transform the model image and sample the resulting visibility function at the same *u*–*v* coordinates that were sampled in both our SUB and VEX SMA observations. The SUB and VEX data were fitted simultaneously using a model that included both the AaAb and B emission regions.

Forward modeling was performed on these data using a Markov Chain Monte Carlo (MCMC) as implemented in the *emcee* package (Foreman-Mackey et al. 2013). Figure 3 shows

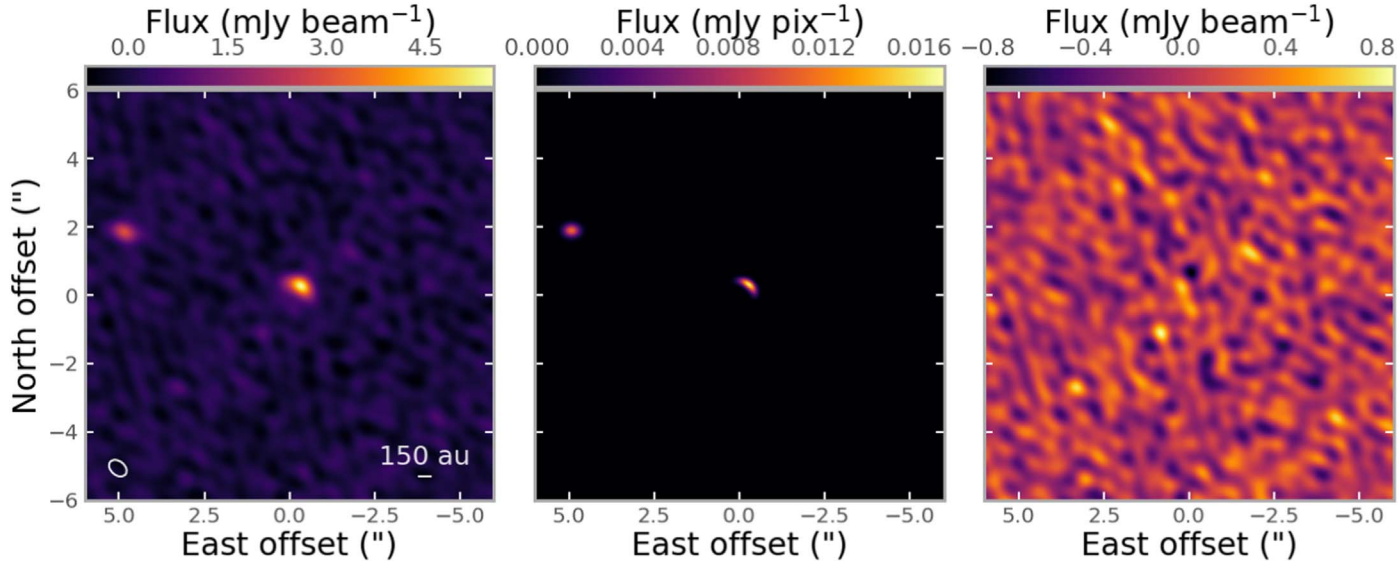


**Figure 4.** Left: natural-weighted image of VEX observations of HD 34700. Middle: best-fit model as determined by MCMC fitting, using parameter values shown in Table 2. Right: residual of the best-fit model.

**Table 2**
Best-fit Parameter Values Summary

| Parameter | Value |
|---|---|
| Trap radius ($r_c$) (au) | $155^{+11}_{-7}$ |
| Trap radial FWHM (au) | $72^{+14}_{-15}$ |
| Azimuthal peak location[a] ($\theta_c$) | $-110° \pm 2°$ |
| Azimuthal FWHM | $64^{\circ+8}_{-7}$ |
| Total flux (mJy) | $7.9 \pm 0.2$ |
| Inclination of trap[b] | $<47°$ |
| Companion flux (mJy) | $3.6 \pm 0.2$ |
| R.A. offset of companion (arcsec) | $4.92 \pm 0.02$ |
| Decl. offset of companion (arcsec) | $1.87 \pm 0.01$ |
| Companion FWHM (au) | $136^{+21}_{-22}$ |
| Position angle of companion | $89^{\circ+9}_{-8}$ |
| Inclination of companion[b] | $>15°$ |
| R.A. SUB offset (arcsec) | $0.09 \pm 0.03$ |
| Decl. SUB offset (arcsec) | $0.05 \pm 0.04$ |

**Notes.** Offsets and distances are measured from the estimated position of the central binary, corresponding to the phase center of the VEX observations. Reported uncertainties correspond to the 16th and 84th percentiles of the posterior probability distribution.
[a] Measured where the positive angular direction is counterclockwise from the positive $x$-axis in the orbital plane.
[b] Posterior probability distributions for both the inclination of the central disk and the companion disk were non-Gaussian in shape and skewed toward 0° and 90°, respectively, and therefore are reported as $3\sigma$ upper and lower limits.

the data, the model, and the residuals that resulted. The value of $\chi^2$ calculated by comparing the sampled data and model visibilities was used to calculate the likelihood function, assumed to be $\propto e^{-\chi^2/2}$. Uniform priors were chosen to enable the MCMC walkers to explore a wide but plausible range of the parameter space, with the uniform prior ranges being, in general, much broader than the width of the converged posterior probability distributions. The exception is the geometric parameters, for which the parameter space is bound by definition (e.g., inclination is defined between 0° and 90° and position angle between −180° and 180°). Fourteen parameters, listed in Table 2, were fit using *emcee*. Beyond the geometric parameters of the Gaussian models and the flux, the offset of the SUB observations from the VEX observations in R.A. and decl. were also fitted as nuisance parameters. The position angle of the disk around the inner AaAb binary is fixed to 69°, as reported in Monnier et al. (2019).

Table 2 contains the parameter values that yielded the best fit to the data, listed as the 50 ± 34th percentile of the posterior probability distributions. The reduced $\chi^2$ of this model is 1.02. We estimate the dust emission to be at a distance of ∼155 au from the central binary and lie on a plane that is inclined by less than 47° from face-on. This places the emission at a location consistent with the cavity described by Monnier et al. (2019) based on NIR imaging, as shown in Figure 3, and at an inclination consistent with the value of 42° inferred from the same NIR observations.

Our visibility fitting indicates that the dust emission around both HD 34700AaAb and the companion HD 34700B are spatially resolved, with the trap extending 72 au in radius and 64° in azimuth and the HD 34700B emission having a Gaussian FWHM diameter of ∼102 au. This is confirmed by the observed and model visibility profiles of the emission around both HD 34700AaAb and B (Figure 5), showing a significant decrease in their real part as a function of $u$–$v$ distance. Our fitting also confirms that the centroid of the companion emission is consistent with the known location of HD 34700B from previous optical observations (e.g., Sterzik et al. 2005).

Additionally, the close matching between the modeled value for the total integrated flux of the central emission and the observed value (modeled $= 7.9 \pm 0.2$ mJy, observed $= 7.4 \pm 1.6$ mJy) indicates that the VEX observations did not miss significant large-scale structure due to the lack of short baselines.

### 3.2. Dust Mass Estimate

The dust emission around the central binary is resolved, as supported by the modeling in Section 3.1 and proven by the $u-v$ profiles shown in Figure 5. To calculate the dust mass around the central binary and HD 34700B, we assume that the dust grains act as modified blackbodies and emit according to

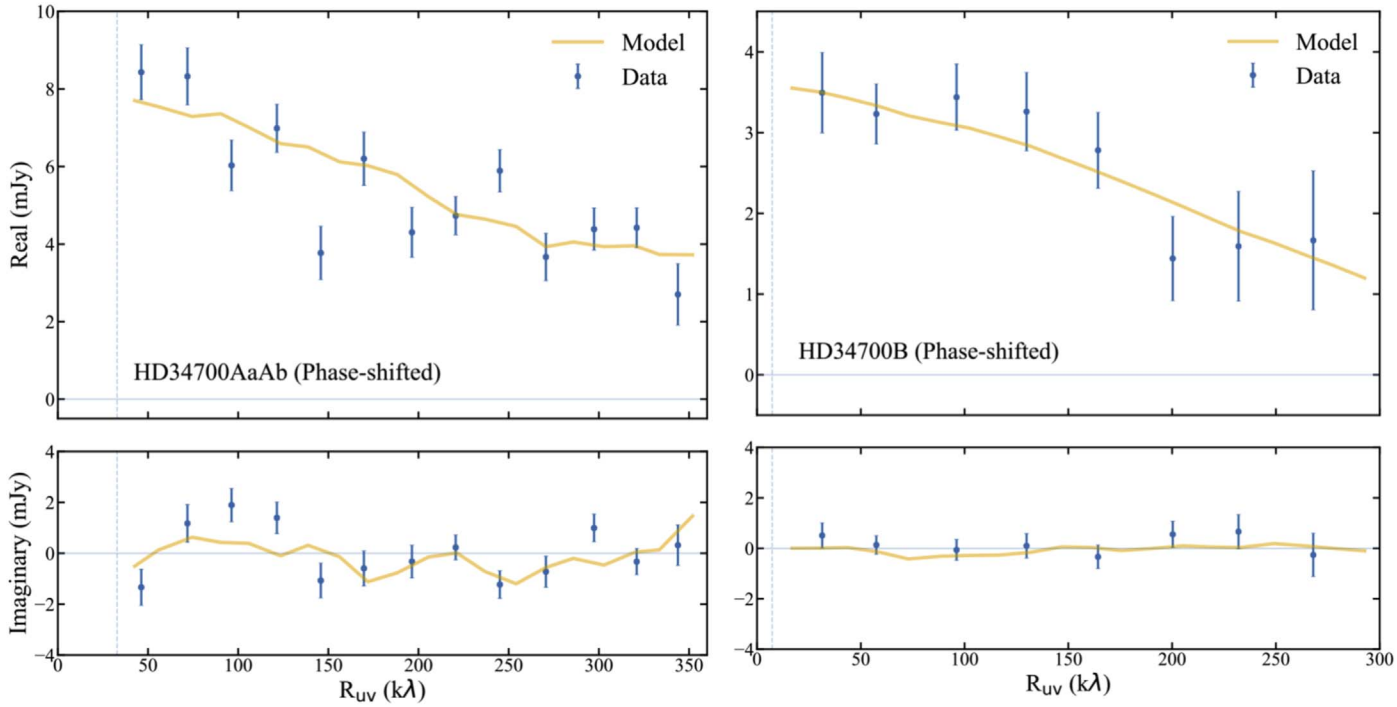


**Figure 5.** Real (top) and imaginary (bottom) parts of the observed visibilities as a function of *u*–*v* distance. Left: visibility function of the emission around the inner binary HD 34700AaAb after subtracting the best-fit emission around B and phase shifting to the on-sky location of the offset emission region. Right: deprojected visibility profile of the emission around the companion HD 34700B after subtracting the best-fit emission around AaAb and phase shifting to the on-sky location of HD 34700B. The best-fit inclination and PA (Table 2) of B were used to apply the deprojection, following the method of, e.g., Hughes et al. (2007). For both HD 34700AaAb and B, the real part is decreasing significantly as a function of *u*–*v* distance, indicating that the emission is spatially resolved by the SMA baselines.

the Planck function. We can then derive a total dust mass from the observed continuum emission assuming that the dust is optically thin,

$$M_{\rm dust} = \frac{F_\nu d^2}{\kappa_\nu B_\nu T_{\rm dust}}, \quad (2)$$

where $F_\nu$ is the measured flux, $d$ is the distance to the system, and $\kappa_\nu$ is the dust grain opacity, assumed to be 10 $\rm cm^2\,g^{-1}$ at 1000 GHz and scaled to the frequency of our observations (230 GHz) using an opacity power-law index $\beta = 1$ (Beckwith et al. 1990; Cazzoletti et al. 2018). For temperatures between 10 and 75 K, we obtain optically thin dust masses between $5.7 \pm 1.2$ and $72 \pm 15\ M_\otimes$ for the emission around the central binary and $2.8 \pm 0.7$ and $35 \pm 9\ M_\otimes$ for the emission around HD 34700B.

To check our optically thin assumption, in the absence of further substructure within the beam of our observations, we can estimate the optical depth from the observed peak intensity. For dust, the optical depth $\tau_\nu$ is related to the intensity $I_\nu$ and the predicted Planck distribution $B_\nu$ by

$$I_\nu = (1 - e^{-\tau_\nu}) B_\nu. \quad (3)$$

For our observed peak continuum intensity around the central binary $I_\nu$ of 5.5 mJy $\rm beam^{-1}$ and a temperature of 30 K, we find that $\tau_\nu \approx 0.02$, which would indicate that the dust emission around the central binary is optically thin. Additionally, the peak flux of the emission around HD 34700B is 2.95 mJy $\rm beam^{-1}$, which, for an assumed temperature of 30 K, yields an optical depth of 0.1. Therefore, all dust emission in this system is most likely to be optically thin as long as no further substructure is present within the observed emission.

### 3.3. CO Gas Mass Estimate

In the optically thin approximation, we can also estimate a CO gas mass $M_{\rm CO}$ from our measured CO integrated flux $F_{2-1}$,

$$M_{\rm CO} = \frac{4\pi m d^2}{h\nu_{2-1}A_{2-1}} \frac{F_{2-1}}{x_2}, \quad (4)$$

where $m$ is the mass of the CO molecule, $d$ is the distance to the system, $\nu_{2-1}$ is the rest frequency of the line, $h$ is Planck's constant, $A_{2-1}$ is the Einstein $A$ coefficient for the transition, and $x_2$ is the fraction of CO molecules that are in the upper energy level of the transition. The $^{12}$CO mass calculation is performed assuming a temperature of 38 K, as derived at the end of this section. The fractional population, $x_j$, depends on the relative excitation of energy levels within the $^{12}$CO molecule. Assuming LTE, levels are populated according to the Boltzmann distribution following Equation (5), using the Einstein $A$ coefficient value of $A_{2-1} = 6.91 \times 10^{-7}$ $\rm s^{-1}$ (Schoeier et al. 2005). This yields a fractional population of the second energy level of $x_2 = 0.309$, calculated from

$$x_j = \frac{N_j}{N_{\rm tot}} = \frac{g_j}{Z} e^{-E_j/kT_k}, \quad (5)$$

where $g_j$ is the degeneracy of the $j$th level, $E_j$ is the energy of that level, and $Z$ is the partition function, defined as $Z = \sum g_i e^{-E_i/kT_k}$. The optically thin calculation leads to a $^{12}$CO gas mass of $0.020 \pm 0.004\ M_\otimes$. This should be considered a lower limit if the emission is instead optically thick.

To test the latter, here we attempt to constrain the optical depth of the $^{12}$CO emission. This can be estimated using the

definition of optical depth,

$$\tau_{\rm CO} = \frac{h\nu}{4\pi\Delta\nu}(x_1 B_{12} - x_2 B_{21}) N_{\rm CO}, \quad (6)$$

where $\Delta\nu$ represents the line width due to Doppler broadening, $B_{12}$ and $B_{21}$ are the Einstein $B$ coefficients, $N_{\rm CO}$ is the column density of CO molecules, and $x_1$ and $x_2$ are the fraction of molecules in the first and second rotationally excited energy levels as calculated from Equation (5). We calculate the column density by approximating the region of CO emission to be a uniform density, axisymmetric disk with the radius and radial width of the trap (∼155 au with a width of 72 au, as determined in Section 3.1) at the same inclination as the trap (24°, consistent with the constraint of <47° found in Section 3.1). Using the measured CO mass of ∼0.02 $M_\otimes$, the optical depth is approximately 19, which would indicate that the CO gas is optically thick and therefore that our mass (and optical depth) is an underestimate.

The 3$\sigma$ integrated line flux upper limit for $^{13}$CO is 0.79 Jy km s$^{-1}$. This is 9.1 times lower than our $^{12}$CO integrated line flux of 7.2 ± 1.4 Jy km s$^{-1}$. Using this lower limit on the $^{12}$CO/$^{13}$CO line ratio, we can use the following expression to crudely estimate the optical depths (as used in Lyo et al. 2011):

$$R = \frac{T_R(^{12}\mathrm{CO})}{T_R(^{13}\mathrm{CO})} = \frac{1 - e^{-\tau_{12\mathrm{CO}}}}{1 - e^{-\tau_{13\mathrm{CO}}}} = \frac{1 - e^{-\tau_{12\mathrm{CO}}}}{1 - e^{-\tau_{12\mathrm{CO}}/X}}. \quad (7)$$

This yields a maximum optical depth of 7 for $^{12}$CO and 0.1 for $^{13}$CO, assuming that the isotopes share the same spectra–spatial morphology and excitation conditions, and that the interstellar value of $X = \frac{^{12}\mathrm{CO}}{^{13}\mathrm{CO}} = 60$ (Wilson & Rood 1994) applies.

Because the $^{12}$CO gas is optically thick, we can assume $I_\nu \approx B_\nu(T)$ and use the peak intensity to calculate a temperature estimate for the $^{12}$CO gas. The peak single-channel intensity was 0.24 Jy beam$^{-1}$; using this, we calculate the $^{12}$CO temperature at the peak intensity location to be 38 K.

Assuming that the $^{13}$CO emission is optically thin, we can calculate an upper limit on its mass using Equation (4). This yields a value of 3.5 × 10$^{-3}$ $M_\otimes$ of $^{13}$CO at a temperature of 38 K. By combining this with the interstellar ratio of $X = \frac{^{12}\mathrm{CO}}{^{13}\mathrm{CO}} = 60$ (Wilson & Rood 1994), we can also calculate an upper limit on the $^{12}$CO gas mass. This yields a value of 0.2 $M_\otimes$ of $^{12}$CO. We can therefore conclude that the total CO gas mass is between the lower limit of 0.02 $M_\otimes$ (determined from only $^{12}$CO observations) and the upper limit of 0.2 $M_\otimes$ (determined from both $^{12}$CO and $^{13}$CO observations).

## 4. Discussion

The HD 34700 system consists of a tight, eccentric ($e \approx 0.25$) central binary of two ∼2 $M_\odot$ stars (AaAb) and two distant companions, thought to be a part of the system due to their shared radial velocity: HD 34700B at a projected separation of 1850 au and HD 34700C at a projected separation of 3300 au (Torres 2004; Sterzik et al. 2005; Monnier et al. 2019). These new 1.3 mm SMA observations show a Keplerian disk of CO gas and an azimuthally asymmetric gathering of dust grains ≈1 mm in size around the central binary, as well as dust emission presumed to be a disk consistent with the location of HD 34700B.

Previous observations of this system by Monnier et al. (2019) at NIR wavelengths showed a disk with spiral arms and a broad cavity around the central AaAb binary. These observations place the HD 34700 system among a growing list of systems shown to have a strongly asymmetric distribution of large dust grains as imaged at (sub)mm wavelengths (e.g., Oph IRS 48, V 1247 Ori, LkHα 330, MWC 758, and HD 135344B; Isella et al. 2013; van der Marel et al. 2013; Follette et al. 2015; Marino et al. 2015; Akiyama et al. 2016; Fuente et al. 2017; Kraus et al. 2017; Cazzoletti et al. 2018), some of which also show a large cavity and spiral features in the NIR. Many causes are proposed for these continuum asymmetries and/or spiral arms, including planets, vortices, gravitational instability, and binary dynamics, which we will discuss in Section 4.1.

The azimuthally asymmetric dust emission observed around the AaAb binary is evidence for dust trapping taking place in this circumstellar disk. If a pressure maximum arises, large grains are more sensitive than small grains to this pressure gradient and can become trapped. Therefore, the detection of this compact emission in (sub)millimeter wavelengths but not NIR observations is indicative of dust trapping. The congregation of large grains in this dust trap can lead to the formation of planetesimals, and it additionally offers a solution to the so-called "radial drift problem," where large (>1 mm) grains rapidly drift inward toward the star (e.g., Whipple 1972; Weidenschilling 1977; van der Marel 2019).

In other systems with evidence for dust traps, the azimuthal asymmetries were detected at smaller radii compared to HD 34700 (∼155 au). In Oph IRS 48, the dust trap was at a distance between 45 and 80 au (±9 au; van der Marel et al. 2013). In HD 135344B, the crescent-shaped asymmetry was modeled to be located at roughly 80 au (Cazzoletti et al. 2018). Our cavity is significantly larger, at a distance of 155 au, placing this among the most distant asymmetries yet detected around young stars. This larger distance to the star (or in this case, the central pair of stars) may imply different formation mechanisms. Observations also find a correlation between the mass of a star and the radius of its disk in the millimeter continuum (Tripathi et al. 2017; Andrews et al. 2018). Simulations of disk formation show disk radii growing on a timescale as short as $10^4$ yr, with larger radii around higher-mass stars (Bate 2018). It is possible that the combined mass of the AaAb binary is sufficiently high to explain the large size of the cavity and the distance between the central binary and the compact emission region.

This work also reports the new detection of the dust disk around HD 34700B, the distant companion. The FWHM of the 2D Gaussian fit to the visibilities is 102 au, which places the disk size squarely in the range established by Andrews et al. (2018) for stars of this mass (disk radii between ∼20 and ∼70 au for $M_* \approx 0.7$ $M_\odot$; Andrews et al. 2018; Monnier et al. 2019). Because the disk size appears to be consistent with that of single stars similar to HD 34700B in mass and temperature, it seems that the inner AaAb binary may not have significantly impacted the evolution of the disk around HD 34700B. Additionally, the inclination of the disk around B is likely different than that of the inner circumbinary disk, implying significant misalignment (however, both inclinations are poorly constrained by this model; see footnote in Table 2). Therefore, it is likely that the AaAb and B pair formed through turbulent fragmentation and/or capture (Bate 2018) and, considering the large distance between them, evolved mostly independently of one another. No substructure is resolved in the HD 34700B

disk, but future higher-resolution observations could attempt to detect substructures around the distant companion.

The most similar young star system to HD 34700 in architecture and disk morphology is HD 142527. It is a binary composed of a 2.2 ± 0.3 $M_\odot$ star and a 0.1–0.4 $M_\odot$ star in a binary with eccentricity $e = 0.5 \pm 0.2$, estimated to have an age of $5^{+8}_{-3}$ Myr (Verhoeff et al. 2011; Biller et al. 2012; Lacour et al. 2016). The disk observed around the binary in HD 142527 has one of the largest eccentric circumbinary cavities known to date that is depleted in millimeter-sized grains but not fully depleted in small dust and gas (Casassus et al. 2012, 2013; Rameau et al. 2012; Canovas et al. 2013; Avenhaus et al. 2017). At the edge of this cavity, there is a large crescent-shaped azimuthal asymmetry in the millimeter continuum that has been interpreted as a dust trap (Casassus et al. 2013, 2015; Fukagawa et al. 2013), although it could potentially be caused by an eccentric central cavity (Ataiee et al. 2013; Price et al. 2018). The HD 142527 disk also exhibits a spiral pattern in IR observations, with spiral arms beginning at the edge of the cavity (Casassus et al. 2012; Avenhaus et al. 2014, 2017). A prominent spiral arm in the IR is seen to have a radially shifted counterpart in $^{12}$CO emission, as well as other spiral arms traced by the CO gas (Fukagawa et al. 2006; Christiaens et al. 2014). The cavity also has a double shadow, thought to be cast by a misaligned inner disk (Avenhaus et al. 2014; Marino et al. 2015). This is similar to the darkening seen in HD 34700 AaAb's disk by Uyama et al. (2020).

Although HD 142527 shares many similarities with HD 34700, there are a few key differences between these systems. The semimajor axis of the HD 142527 binary is $14^{+12}_{-5}$ au (Biller et al. 2012), much larger than the value of ∼0.25 au calculated for HD 34700. Additionally, the mass ratio for the central binary of HD 34700 is close to 1, whereas the mass ratio for HD 142527 is ∼0.1 (Verhoeff et al. 2011). The larger separation of HD 142527 translates to a larger region where stable orbits cannot occur around the central binary. Using the results of the dynamical study of binaries by Holman & Wiegert (1999) and the systems' semimajor axes, mass ratios, and eccentricities, we obtain that the smallest stable orbit around the central HD 142527 binary is ∼53 au, while the smallest stable orbit around HD 34700AaAb is ∼0.8 au. Therefore, the very different binary orbits between the two systems imply that, while HD 142527's eccentric, wider separation stellar companion can explain most of the disk features, HD 34700's inner AaAb binary separation is too small to significantly affect both the disk at 100 au and any companions with semimajor axes greater than 1 au, potentially indicating the need for a third body within the cavity (see Section 4.1.3).

### 4.1. Potential Origin of Observed Structure

#### 4.1.1. Central Cavity

The inner AaAb binary is expected to truncate the disk at a radius of approximately two to three times the binary separation (Artymowicz & Lubow 1994). The inner binary has an eccentricity of roughly 0.25 (Torres 2004), which will affect the truncation of the disk (Miranda & Lai 2015). Using the relations described in Miranda & Lai (2015), we must consider the disk–binary relative inclination and the binary's semimajor axis and eccentricity to determine the expected truncation radius. The inclination of the binary is constrained spectroscopically by Torres (2004), stating that $M_* \sin^3(i) \approx 0.53 M_\odot$, which, when combined with the new masses determined by Monnier et al. (2019), yields a central binary inclination of $i \approx 40°$ or 140°. The former value is consistent with the inclination of the dust disk around the central binary (<47° as determined by our model in Section 3.1 and ∼40° from NIR observations; Monnier et al. 2019). We can then use the relation between cavity size and binary separation established in Miranda & Lai (2015) for a given relative disk–binary inclination to estimate the cavity size that would be produced by the inner binary. Considering the inclination of 40° or 140°, the binary semimajor axis would be $a \sim 0.25$ au based on the spectroscopic observations of Torres (2004). The ratio $r_{\rm cavity}/a$ predicted by the models is 2.1 for the given inclination, mass ratio, and eccentricity, which means that the cavity that would be produced by the inner binary dynamics would be much smaller ($r_{\rm cavity} \approx 0.53$ au) than the observed cavity ($r \approx 175$ au; Monnier et al. 2019). Therefore, even considering its eccentricity, the AaAb binary cannot be responsible for the large cavity. This motivates the introduction of a tertiary massive companion within the cavity, as discussed in Section 4.1.3.

#### 4.1.2. External Companion Dynamics

An external companion in a multiple system can interact with an inner circumbinary disk and potentially influence the substructures within that disk. The HD 100453 system (described in Rosotti et al. 2020) has spiral arms in scattered light, as well as in the millimeter continuum, that have been determined to most likely originate from interactions with the known outer companion. In the HD 34700 system, however, the tertiary companion is much more distant than the one in HD 100453 (projected separation 1850 au versus 110 au), likely too far away to truncate the circumbinary disk and produce the spiral arms seen in scattered light (Rosotti et al. 2020). The CO gas emission detected around the central binary in these observations does not extend out to nearly the same distance as HD 34700B, so the only influence this distant companion could have on the inner circumbinary disk would be if HD 34700B was nearer to the central binary in the past or its orbit was highly eccentric.

"Flyby" encounters with such a perturber can cause spiral structures and asymmetries (Cuello et al. 2020). The perturber can also capture some of the disk material and produce tidal streams (as seen in, for example, RW Aur as described in Dai et al. 2015). While past capture of circumbinary material could explain the presence of a disk around HD 34700B, there is no evidence for a tidal stream in our SMA CO observations. However, our observed disk sizes for AaAb and B are consistent with those observed around single stars, which would argue against a close, disruptive flyby in HD 34700's past. Nonetheless, future dynamical simulations are needed to test this scenario in detail.

Additionally, the fourth star, HD 34700C, as well as the potential fifth member of the system suggested by Monnier et al. (2019), could potentially affect the dynamics of the system, but the lack of information on the true 3D geometry of the system limits any speculation about that. Because these companions are at distances even greater than that of HD 34700B, they are unlikely to have had a significant influence on the circumbinary disk unless they have a very eccentric orbit or passed much nearer to the central binary in the distant past.

#### 4.1.3. Internal Companion Dynamics

The presence of a low-mass companion within the dust cavity was proposed by Monnier et al. (2019) to explain the presence of the cavity. They performed a targeted simulation, where they found that a 50 $M_{\rm Jupiter}$ companion would produce the cavity and the observed discontinuity seen in the NIR but would not reproduce the spiral arms. To reproduce the spiral arm structure seen in NIR scattered-light observations, it would require either multiple companions or an eccentric companion (Monnier et al. 2019). An inner eccentric companion can trigger multiple outer spirals, as shown by simulations and radiative transfer modeling in Calcino et al. (2020).

Additional observations by Uyama et al. (2020) placed limits on the companion mass of 12 $M_{\rm Jupiter}$ at 0.″3 (or ∼107 au) and 5 $M_{\rm Jupiter}$ at 0.″75 (or ∼267 au). A giant companion within the limits proposed by Uyama et al. (2020) could be consistent with the presence of CO and small grain emission interior to the cavity (Dong et al. 2012; Zhu et al. 2012). The edge of a cavity produced by such a massive planet/companion would be subject to Rossby wave instability (Papaloizou & Pringle 1984; Lovelace et al. 1999). If the disk viscosity is sufficiently low (Zhu & Stone 2014), this will produce a long-lived anticyclonic vortex in the gas with a gas pressure maximum at its center. This gas pressure maximum will cause dust trapping with a preference for larger grains (Weidenschilling 1977; Barge & Sommeria 1995; Birnstiel et al. 2013) and potentially explain our observed major asymmetry in the millimeter continuum emission. Therefore, all observed structure in this system seems plausibly created by a massive planet or brown dwarf just interior to the cavity edge.

Based on calculations in Holman & Wiegert (1999), the eccentricity of the central binary would only affect the long-term stability of a companion if it is located within 0.8 au of the central binary. This is much smaller than the cavity of interest in this system (and the radii relevant to the mass limits in Uyama et al. 2020); therefore, it is possible for a companion to be at a stable orbit at a wide range of semimajor axes within the cavity. Detailed dynamical simulations are needed to test whether a planet within the mass limits imposed by Uyama et al. (2020) would be capable of reproducing all of the observed features, including the cavity size, CO and small dust inward filtering, and high-contrast azimuthal millimeter-dust trapping.

If a planet is invoked as the cause of the cavity and asymmetry, then it indicates that the formation of a massive companion as distant as 160 au must have taken place rapidly within the system age of 5 Myr, unless the orbit of the companion is highly eccentric. This rapid companion formation could have been facilitated by a very massive protostellar disk, as is commensurate with the binary pair of massive stars at its center.

#### 4.1.4. Gravitational Instability

If the protostellar disk was indeed very massive in the past, it may have been gravitationally unstable (see Kratter & Lodato 2016 for a review of gravitational instability).

The spiral arms observed in scattered light by Monnier et al. (2019) are a specific prediction of gravitational instability models (Dipierro et al. 2014; Hall et al. 2019). However, Monnier et al. (2019) argued that, based on radiative transfer modeling, the Toomre $Q$ parameter is greater than 25 everywhere in the disk, and therefore it is unlikely that the disk is gravitationally unstable at present. Kratter & Lodato (2016) stated that disks are generally not gravitationally unstable unless the $\frac{M_d}{M_*}$ ratio is greater than $10^{-2}$. To calculate the total disk mass, we use our calculated CO mass limits from Section 3.3, assume an $H_2$/CO ratio of $10^4$, and add the dust mass by assuming a gas–dust ratio (by mass) of 10. The lower limit of the total estimated disk mass is $3.6 \times 10^{-5}$ $M_\odot$, and the upper limit is $4.3 \times 10^{-4}$ $M_\odot$. For this system, this yields $\frac{M_d}{M_*} \geqslant 10^{-4}$ using the lower limit on the CO mass or $\frac{M_d}{M_*} \geqslant 10^{-3}$ using the upper limit on the CO mass. This strongly implies that the disk is not gravitationally unstable at present, unless it is more massive than our assumptions allow. Even if the disk is not gravitationally unstable at present, it may have been gravitationally unstable in the past when it was more massive. This could cause the rapid and early formation of the massive companion proposed by Monnier et al. (2019) to explain the observed substructure.

## 5. Summary and Conclusions

In this paper, we present new high-resolution (∼0.″5) SMA observations of the HD 34700 multiple system. We discover azimuthally asymmetric emission in the 1.3 mm continuum around the central AaAb binary, which we interpret as evidence for dust trapping. We also report the discovery of dust emission associated with a protoplanetary disk around the distant companion HD 34700B. We determine that the inclination of the AaAb circumbinary disk is consistent with being aligned with the inclination of the plane of the central binary as spectroscopically constrained by Torres (2004).

The substructures observed both in (sub)millimeter and NIR observations (Monnier et al. 2019) can be explained by the presence of a companion in the circumbinary disk (or companions) that must have formed within 5 Myr. To form a massive companion so rapidly, it is possible that the disk around HD 34700AaAb was massive enough to be gravitationally unstable in the past. Our calculated disk mass, inferred from CO emission, implies that the disk is not gravitationally unstable at present. As mentioned in Monnier et al. (2019), a deeper search for point sources within ∼170 au from the central binary would be necessary to confirm the presence of a young companion that could potentially explain the dust trap observed in millimeter wavelengths and the spiral arms seen in scattered light. The observed structures indicate that this system is an interesting candidate for future high-sensitivity, high angular resolution Atacama Large Millimeter/submillimeter Array observations to enable a better characterization of the disk and better constraints on the origin of the observed disk features.

J.D.M. and E.A.R. acknowledge NSF AST 1830728. This work has made use of data from the European Space Agency (ESA) mission Gaia (Gaia Collaboration et al. 2018), processed by the Gaia Data Processing and Analysis Consortium (DPAC). Funding for the DPAC has been provided by national institutions, in particular the institutions participating in the Gaia Multilateral Agreement. This research has also made use of the SIMBAD database (Wenger et al. 2000), operated at CDS, Strasbourg, France, and NASA's Astrophysics Data System Bibliographic Services.

The authors also wish to acknowledge the cultural significance of the summit of Maunakea to the indigenous Hawaiian people. We are fortunate to have the privilege to

observe from this mountain. We also thank the anonymous referee for useful commentary.

## ORCID iDs

Peyton Benac https://orcid.org/0000-0002-9384-5365
Luca Matrà https://orcid.org/0000-0003-4705-3188
David J. Wilner https://orcid.org/0000-0003-1526-7587
Marìa J. Jimènez-Donaire https://orcid.org/0000-0002-9165-8080
J. D. Monnier https://orcid.org/0000-0002-3380-3307
Tim J. Harries https://orcid.org/0000-0001-8228-9503
Anna Laws https://orcid.org/0000-0002-2145-0487
Evan A. Rich https://orcid.org/0000-0002-1779-8181
Qizhou Zhang https://orcid.org/0000-0003-2384-6589

## References

Akiyama, E., Hashimoto, J., Liu, H. B., et al. 2016, AJ, 152, 222
Andrews, S. M., Huang, J., Pérez, L. M., et al. 2018, ApJL, 869, L41
Andrews, S. M., Terrell, M., Tripathi, A., et al. 2018, ApJ, 865, 157
Artymowicz, P., & Lubow, S. H. 1994, ApJ, 421, 651
Ataiee, S., Pinilla, P., Zsom, A., et al. 2013, A&A, 553, L3
Avenhaus, H., Quanz, S. P., Schmid, H. M., et al. 2014, ApJ, 781, 87
Avenhaus, H., Quanz, S. P., Schmid, H. M., et al. 2017, AJ, 154, 33
Barge, P., & Sommeria, J. 1995, A&A, 295, L1
Bate, M. R. 2018, MNRAS, 475, 5618
Beckwith, S. V. W., Sargent, A. I., Chini, R. S., et al. 1990, AJ, 99, 924
Biller, B., Lacour, S., Juhász, A., et al. 2012, ApJL, 753, L38
Birnstiel, T., Dullemond, C. P., & Pinilla, P. 2013, A&A, 550, L8
Bruderer, S., van der Marel, N., van Dishoeck, E. F., et al. 2014, A&A, 562, A26
Calcino, J., Christiaens, V., Price, D. J., et al. 2020, MNRAS, 498, 639
Canovas, H., Ménard, F., Hales, A., et al. 2013, A&A, 556, A123
Casassus, S., Perez, S., Jordán, M. A., et al. 2012, ApJL, 754, L31
Casassus, S., van der Plas, G. M., Perez, S., et al. 2013, Natur, 493, 191
Casassus, S., Wright, C. M., Marino, S., et al. 2015, ApJ, 812, 126
Cazzoletti, P., van Dishoeck, E. F., Pinilla, P., et al. 2018, A&A, 619, A161
Christiaens, V., Casassus, S., Perez, S., et al. 2014, ApJL, 785, L12
Cuello, N., Louvet, F., Mentiplay, D., et al. 2020, MNRAS, 491, 504
Dai, F., Facchini, S., Clarke, C. J., et al. 2015, MNRAS, 449, 1996
Dipierro, G., Lodato, G., Testi, L., et al. 2014, MNRAS, 444, 1919
Dong, R., Hashimoto, J., Rafikov, R., et al. 2012, ApJ, 760, 111
Follette, K. B., Grady, C. A., Swearingen, J. R., et al. 2015, ApJ, 798, 132
Foreman-Mackey, D., Hogg, D. W., Lang, D., et al. 2013, PASP, 125, 306
Fuente, A., Baruteau, C., Neri, R., et al. 2017, ApJL, 846, L3
Fukagawa, M., Tamura, M., Itoh, Y., et al. 2006, ApJL, 636, L153
Fukagawa, M., Tsukagoshi, T., Momose, M., et al. 2013, PASJ, 65, L14
Gaia Collaboration, Brown, A. G. A., Vallenari, A., et al. 2018, A&A, 616, A1
Hall, C., Dong, R., Rice, K., et al. 2019, ApJ, 871, 228
Ho, P. T. P., Moran, J. M., & Lo, K. Y. 2004, ApJL, 616, L1
Holman, M. J., & Wiegert, P. A. 1999, AJ, 117, 621
Hughes, A. M., Wilner, D. J., Calvet, N., et al. 2007, ApJ, 664, 536
Isella, A., Pérez, L. M., Carpenter, J. M., et al. 2013, ApJ, 775, 30
Juhász, A., & Rosotti, G. P. 2018, MNRAS, 474, L32
Kratter, K., & Lodato, G. 2016, ARA&A, 54, 271
Kraus, S., Kreplin, A., Fukugawa, M., et al. 2017, ApJL, 848, L11
Lacour, S., Biller, B., Cheetham, A., et al. 2016, A&A, 590, A90
Lovelace, R. V. E., Li, H., Colgate, S. A., et al. 1999, ApJ, 513, 805
Lyo, A.-R., Ohashi, N., Qi, C., et al. 2011, AJ, 142, 151
Lyra, W., & Lin, M.-K. 2013, ApJ, 775, 17
Marino, S., Casassus, S., Perez, S., et al. 2015, ApJ, 813, 76
Marino, S., Perez, S., & Casassus, S. 2015, ApJL, 798, L44
McMullin, J. P., Waters, B., Schiebel, D., et al. 2007, in ASP Conf. Ser. 376, Astronomical Data Analysis Software and Systems, ed. R. A. Shaw et al. (Tuscon, AZ: ASP), 127
Miranda, R., & Lai, D. 2015, MNRAS, 452, 2396
Monnier, J. D., Harries, T. J., Bae, J., et al. 2019, ApJ, 872, 122
Papaloizou, J. C. B., & Pringle, J. E. 1984, MNRAS, 208, 721
Pinilla, P., Benisty, M., & Birnstiel, T. 2012, A&A, 545, A81
Pourbaix, D., Tokovinin, A. A., Batten, A. H., et al. 2004, A&A, 424, 727
Price, D. J., Cuello, N., Pinte, C., et al. 2018, MNRAS, 477, 1270
Rameau, J., Chauvin, G., Lagrange, A.-M., et al. 2012, A&A, 546, A24
Rosotti, G. P., Benisty, M., Juhász, A., et al. 2020, MNRAS, 491, 1335
Schmid, H. M., Joos, F., & Tschan, D. 2006, A&A, 452, 657
Schoeier, F. L., van der Tak, F. F. S., van Dishoeck, E. F., & Black, J. H. 2005, A&A, 432, 369
Sterzik, M. F., Melo, C. H. F., Tokovinin, A. A., et al. 2005, A&A, 434, 671
Tazzari, M., Beaujean, F., & Testi, L. 2018, MNRAS, 476, 4527
Testi, L., Natta, A., Shepherd, D. S., et al. 2003, A&A, 403, 323
Torres, G. 2004, AJ, 127, 1187
Tripathi, A., Andrews, S. M., Birnstiel, T., et al. 2017, ApJ, 845, 44
Uyama, T., Currie, T., Christiaens, V., et al. 2020, ApJ, 900, 135
van der Marel, N. 2019, arXiv:1902.00005
van der Marel, N., van Dishoeck, E. F., Bruderer, S., et al. 2013, Sci, 340, 1199
van der Marel, N., Williams, J. P., Ansdell, M., et al. 2018, ApJ, 854, 177
Verhoeff, A. P., Min, M., Pantin, E., et al. 2011, A&A, 528, A91
Weidenschilling, S. J. 1977, MNRAS, 180, 57
Wenger, M., Ochsenbein, F., Egret, D., et al. 2000, A&AS, 143, 9
Whipple, F. L. 1972, in Nobel Symp. 21, From Plasma to Planet, ed. A. Evilius (New York: Wiley), 211
Wilson, T. L., & Rood, R. 1994, ARA&A, 32, 191
Zhu, Z., Nelson, R. P., Dong, R., et al. 2012, ApJ, 755, 6
Zhu, Z., & Stone, J. M. 2014, ApJ, 795, 53